



Investigation of the effects of boundary layer ingestion engine integration on aircraft thrust requirement

A. Vinz¹ · A. Raichle¹

Received: 19 January 2023 / Revised: 20 December 2023 / Accepted: 31 January 2024
© The Author(s) 2024

Abstract

In order to further the understanding of boundary layer ingestion (BLI) engine integration concepts the DLR project AGATA^{3S} aimed at modelling and evaluating the inhomogeneous inflow into turbofans positioned on either side of the rear fuselage. Besides investigating increased flow-induced blade vibrations as well as the excitation of additional noise sources, a focus within AGATA^{3S} was the assessment of BLI on overall aircraft performance. The present paper discusses the results of a parameter study carried out on the DLR TuLam aircraft in which a UHBR engine was embedded into the rear fuselage to varying degrees in order to understand the relationship between degree of embedding and total aircraft thrust requirement. The TuLam underwing-mounted engine configuration was used as a reference. The performance data as well as the phenomenological effects of BLI engine integration are assessed.

Keywords BLI · Engine integration · Inlet distortion · Degree of embedding parameter study · Actuator disk · DC60 · Shaft power

List of symbols

C_D	Drag coefficient
C_L	Lift coefficient
C_t	Thrust coefficient
l_e	Distance between the center of the fuselage and the center of the engine
f	Sectional load of the blade section, calculated from the curves of lift $C_L(\alpha)$ and drag $C_D(\alpha)$
N	Revolutions per minute
r	Radius or radial distance to the axis of rotation
r_e	Engine radius
r_f	Fuselage radius
q	Dynamic pressure

Subscripts

Conv	Conventional underwing configuration
R1	Front rotor
R2	Aft rotor
AD	Actuator disk
is	Isentropic

Greek symbols

α	Angle of attack
β	Incidence angle
φ	Peripheral Angle
θ	Total temperature ratio
κ	Adiabatic exponent
Π	Total pressure ratio
Ω	Angular velocity

Abbreviation

AD	Actuator disk
BLI	Boundary layer ingestion
DC	Distortion coefficient
DFC	Distributed fans concept
DLR	German aerospace center
DOE	Degree of embedding
MIT	Massachusetts institute of technology
NASA	National aeronautics and space administration
ONERA	Office National d'Etudes et de Recherches Aérospatiales
PFC	Propulsive fuselage concept
PSC	Power saving coefficient
RANS	Reynolds averaged navier stokes
REC	Rear engine concept
UHBR	Ultra high bypass ratio
uRANS	Unsteady Reynolds averaged navier stokes

✉ A. Raichle
axel.raichle@dlr.de

¹ German Aerospace Center (DLR), Institute of Aerodynamics and Flow Technology, Lilienthalplatz 7, 38108 Brunswick, Germany

1 Introduction

Research and development in the aviation industry is largely driven by the goal of increasing the aerodynamic efficiency of aircraft and reducing noise and greenhouse gas emissions. The Advisory Council for Aviation Research and Innovation in Europe has outlined its vision for aviation in its agenda “ACARE Flightpath 2050”. It set the objective to reach 75% reduction in CO₂ emissions and 90% reduction in NO_x emissions per passenger per kilometer as well as 65% reduction in perceptible noise emissions by the year 2050 [1].

In order to meet these requirements, the bypass ratio of the engine is likely to be further increased. This will likely require a design change of future generations of aircraft due to the limited space beneath the wings of a typical low-wing aircraft configuration. The large nacelles of ultra-high bypass ratio engines will result in a significant increase in skin friction drag, which eventually will pose an upper limit to the maximum possible engine size. The application of boundary layer ingestion (BLI) in conjunction with a rear engine concept (REC) by partially integrating the engine into the tail of the airframe can both reduce friction drag and potentially aid in the acoustic shielding of engine noise. It allows the engine to ingest low momentum boundary layer flow, re-energizing the aircraft's wake and reducing the exit velocity required to produce thrust.

Rear mounted BLI engine concepts have been extensively studied. Under NASA sponsorship, MIT developed the D8, an innovative aircraft configuration that integrates engines on top of a flat double-bubble fuselage [2]. An experimental assessment of the aerodynamic benefit of boundary layer ingestion for the D8 configuration found that the benefit, quantified by the difference in required mechanical flow power with boundary layer ingestion compared to the case without boundary layer ingestion, is 8.6% at the simulated cruise conditions when the same propulsors are used for both configurations [3]. A framework for BLI analysis based on the power balance method was then developed. By applying this method to wind tunnel data from the powered D8 aircraft model tests mentioned above, the sources of aerodynamic BLI benefit for a realistic transport aircraft configuration were quantified. BLI was found to reduce the required cruise power by 8.2% for the same propulsors (same nozzle area) [4].

ONERA is developing both novel aircraft concepts and methods that make it possible to evaluate these. The NOVA configurations (Nextgen Onera Versatile Aircraft) feature a wide-body, high-lift fuselage and engines embedded into the fuselage on both sides. They also use the potential of BLI to increase the overall efficiency of the engine-airframe integration [5].

Other important BLI concepts are the Propulsive Fuselage Concept (PFC) and the Distributed Fans Concept (DFC). The Propulsive Fuselage Concept (PFC) consists of an engine surrounding the rear of the fuselage. It is powered either mechanically or electrically by two underwing engines. This concept was investigated within the European project DisPURSAL (Distributed Propulsion and Ultrahigh Bypass Rotor Study at Aircraft Level) [6], CENTRELINE (Concept Validation Study for Hull Wake-Filling Propulsion Integration) [7] as well as the NASA project STARC-ABL (Single-aisle turbo-electric aircraft with aft boundary layer propulsion) [8]. Studies of the STARC-ABL concept were conducted over the full design range of BLI fan size and pressure ratio. The results quantify the power savings from BLI compared to a conventional propulsion system in terms of the power saving coefficient and show a potential energy saving of 11–15% [9].

Engelbrecht et al. investigated the influence of the fuselage transition and axial offset on the inlet distortion and performance of a tail-mounted fan for a short-haul commuter aircraft [10].

The distributed fans concept (DFC) represents the most synergistic solution for propulsion and airframe integration. It utilizes turbo-electric distributed propulsion (TeDP) through a series of electrically driven fans positioned on the rear of a blended wing-body type of configuration. This concept was investigated as part of the NASA project N3-X [11] and the ONERA project DRAGON (Distributed fans Research Aircraft with electric Generators by ONERA) [12]. It is the most technologically complex of the three concepts.

The AGATA^{3S} project also aims to increase the overall efficiency of the aircraft through the tight coupling of engine and fuselage. Unlike most of the previously cited studies, a less disruptive tube-and-wing aircraft configuration was chosen with a modified tail-mounted integration of the engines. This was done to avoid the risks associated with a completely new aircraft layout. This would complicate the assessment of the design changes, e.g., in terms of the structural weight of the aircraft, and introduce uncertainties in terms of certification requirements related to critical failure cases. This includes rotor bursts, that may need to be addressed in configurations with a novel placement of the engines on the airframe.

The engine was placed along the upper side of the aircraft's rear end so that it could ingest and energize the boundary layer air (see Fig. 1).

This design leads to an inhomogeneous engine inflow, which in turn may lead to a reduction in the stable engine operating range and engine efficiency. This must be put in relation to the engine power saved as a result of the reduced drag due to the engine integration.

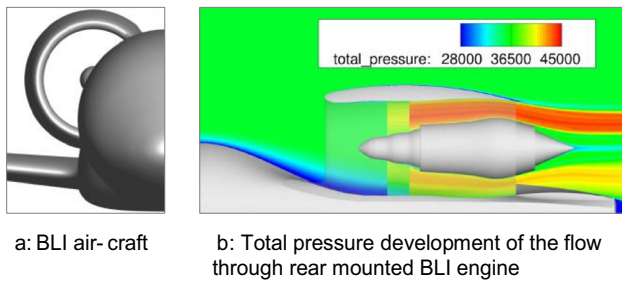


Fig. 1 a BLI air-craft. b Total pressure development of the flow through rear mounted BLI engine

The relationship between the degree of embedding (DOE) and engine thrust saving potential has not yet been extensively researched. Therefore, a parametric study was carried out in which the degree of embedding was varied. This allowed for the assessment of the BLI effect on the overall performance of the aircraft. The engine was integrated with eight different embedding depths.

In this study, the DLR TuLam aircraft, a short to medium-haul transport aircraft with top level aircraft requirements (TLARs) similar to those of an A320-200, was used [13]. The aircraft thrust was trimmed for each configuration to simulate a steady cruise condition ($C_t = C_D$). The differences in required shaft power in each case show the power saving potential of BLI compared to the underwing configuration. This allows a first estimation of the fuel saving potential of a BLI aircraft compared to a conventional underwing configuration. The results are presented and discussed in chapter 3. Chapter 4 discusses flow phenomena that can be traced back to a non-optimized geometry of the embedded engine. Chapter 5 concludes this paper with a summary and an outlook on further work.

2 Methods

2.1 Aircraft and engine model

2.1.1 TuLam aircraft

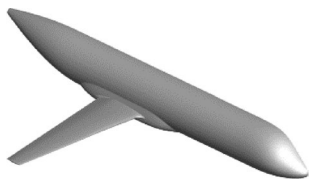
A half-model of the TuLam aircraft was used for this study as it is a design targeted at the market segment of the A320-200, which is one of the most prolific aircraft in service today. The horizontal and vertical tail planes as well as the wing-mounted high-lift devices were not considered in order to simplify the geometric model (see Table 1).

2.1.2 UHBR engine

The aircraft is powered by an ultra-high bypass ratio engine. A generic UHBR nacelle served as the base, with the inlet

Table 1 Main TuLam aircraft parameters

Aircraft	Value
Length	37.57 m
Wing area	122.0 m ²
Wing span	34.0 m



length modified for use with the AGATA^{3S} BLI installation. A counter-rotating fan was used to maximize propulsion efficiency. Counter-rotating fans offer a promising possibility to improve the overall efficiency of aircraft engines. By dividing the pressure rise into two stages, low blade numbers per row and high axial Mach numbers can be achieved. As the second rotor removes most of the swirl, no stator is required for this concept. The absence of stator losses and the low stage loadings enable very high fan efficiencies and allow for high bypass ratios and high propulsive efficiencies [14] (see Table 2).

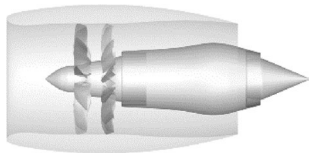
2.1.3 Engine-airframe integration

The engine was positioned as far aft as possible to take advantage of the natural taper of the fuselage tail and ensure a smooth transition from the fuselage into the engine inlet. At the same time, to satisfy safety requirements in the case of rotor burst, the core engines must be shielded from each other in order to minimize the risk of rotor fragments shed from one engine damaging the other turbofan [15]. The rotor burst condition thus sets a limit for the engine position in the upward direction. In combination with the downward constriction of the upper side of the fuselage (see upper black curve in Fig. 2), this means that the engine is simultaneously moved downwards with increasing aft displacement (see dotted curve in Fig. 2).

Moving the engine further aft results in a higher overall mass of the aircraft, due to the need for additional strengthening of the fuselage. A lower limit of the engine position is set by the wing wake, as it must not be ingested by the inlet (see green curve in Fig. 3). The gray dashed

Table 2 Main UHBR engine parameters

Engine	Value
Fan diameter [m]	2.343
Nr. of blades 1/2	10/12
Bypass ratio	17:1
Tot. Press. ratio	1.285



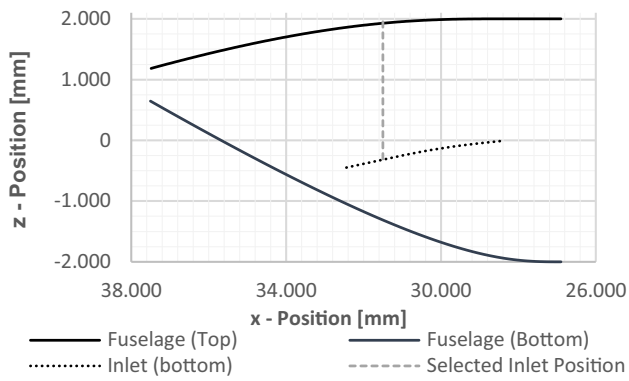


Fig. 2 Engine positioning due to rotor burst constraint

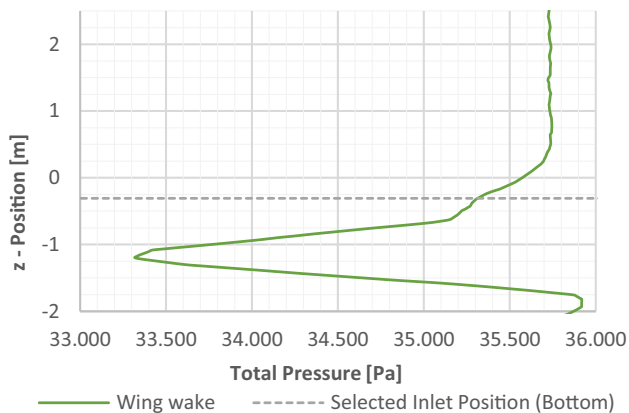


Fig. 3 Wing wake, cruise condition, at angle of attack $\alpha = 2^\circ$ as a natural limit to maximum rear position

line in Figs. 2 and 3 shows the selected engine position based on the convergence of the upper and lower limits with the goal of positioning the engine in the maximum possible tail position.

In order to determine the lower limit of the engine position, simulations were carried out with a clean aircraft configuration without engines both for take-off and for cruise flight in order to investigate the wing wakes. A cut off line, equal for both flight conditions, was drawn above both wing wakes to ensure the circular engine inlet is not affected by those wakes. This is the dotted line which represents the selected inlet position (bottom) in Fig. 3. The total pressure was extracted from a line in 3D space parallel to the z-axis between the top and bottom of the nacelle lip of the UHBR engine located at the $DOE = 30\%$ position.

For the conventional configuration, the engine was mounted in an underwing position. The shape of the nacelle and the inlet remained constant throughout the parametric study and was not optimized for each embedding depth. This led to some undesirable aerodynamic flow features, which are discussed in chapter 4.1 (Fig. 4).

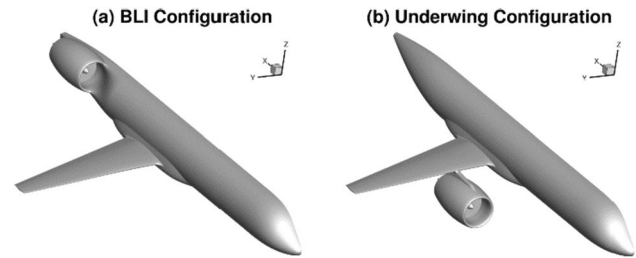


Fig. 4 Investigated aircraft configurations

In order to accurately quantify the depth of embedding of this type of engine integration, the degree of embedding (DOE) was defined.

$$DOE = \frac{r_e + r_f - l_e}{2 \cdot r_e} \quad (1)$$

$$DOE = \frac{\text{masked diameter}}{\text{total diameter}} \quad (2)$$

Due to geometric constraints imposed by the engine and fuselage diameters, the maximum degree of embedding for the TuLAM aircraft is $DOE = 0.55$. In each case, the engine was positioned as high as possible, limited by the rotor burst condition.

2.2 Flight conditions

This study was carried out for cruise flight conditions, as it is the most important flight regime driving the aircraft fuel consumption.

The rotor speed was adjusted in such a way that a balance of forces was achieved and the aircraft moves with a uniform motion. Equation (3) shows the fixed speed ratio between rotor 1 and rotor 2.

$$N_{R1} = -1.267 \cdot N_{R2} \quad (3)$$

In addition, a fixed lift coefficient of $C_L = 0.52$ was retained by adjusting the angle of attack α for each configuration in order to be able to accurately compare the respective efficiency and performance metrics.

2.3 Geometry modelling

CATIA V5 was used to integrate the generic UHBR engine into the tail of the DLR TuLAM aircraft. A parametric model was set up to efficiently create the individual geometries. Common parameters used in the CAD model were the degree of embedding (see Fig. 5), the circumferential position of the engine relative to the fuselage as well as the curvature of the nacelle-body junction (see Figs. 20, 21,

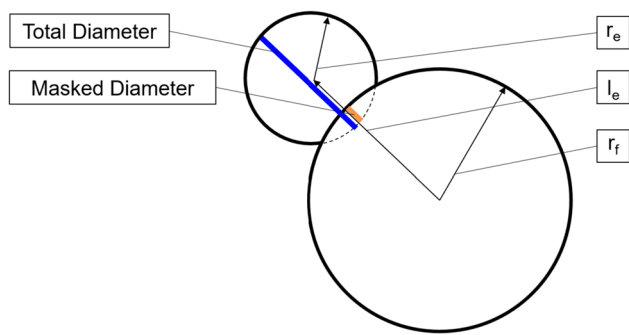


Fig. 5 Definition of degree of embedding (DOE)

Table 3 Cruise flight condition

Cruise flight	Value
Mach number	0.78
Altitude	35,000 ft (10,668 m)
Static temperature	228.8 K ($\Delta T_{isa} = +10$ K)
Static pressure	23,842 Pa
Density	0.363 kg/m ³

22, 23). Regarding the circumferential position, the engine was positioned as far up in the z-direction as possible while still fulfilling the rotor burst condition (see Introduction). Parameters to change engine pitch and yaw angles were also implemented but not used. For reasons of stability, the first-order tangent condition was chosen for the design of the connecting surfaces between fuselage and engine instead of the second-order curvature continuity condition (Table 3).

2.4 Mesh generation

Centaur v15.1 was used to generate the hybrid unstructured grid used for this study [16]. To model the boundary layer properly, 70 layers were extruded from the viscous wall boundaries with an initial height of 1.25×10^{-5} m and a variable growth rate from 1.3 near the wall to 1 in the outer layers, resulting in a total stack height of 375 mm. The mesh consists of mixed cell types such as hexahedrons, tetrahedrons, prisms and pyramids. Where possible, the boundary layer mesh was created with flow-adapted hexahedrons, otherwise prisms were used. Flow-adapted hexahedrons were generated on the wing, the nacelle as well as on the engine surfaces. Initially, the flow domains within the engine were meshed with a structured grid. The results were subsequently compared with those of an unstructured grid. After it was found that they were sufficiently similar work was subsequently continued with a fully unstructured mesh. At concave areas, such as surfaces inside the engine, the number of layers was reduced for geometric reasons. Sources

were placed in aerodynamically critical areas in and around the engine to refine the mesh. The meshes in the BLI study contained approximately 60×10^6 grid points.

2.5 CFD computation

This investigation was performed with the numerical flow solver TAU developed by DLR [17]. It solves the Reynolds-averaged Navier–Stokes equations on unstructured hybrid computational grids using a finite volume discretization with node-based metrics. For the spatial discretization of the convective fluxes, a second-order central differencing scheme with matrix dissipation was used. The viscous fluxes are discretized by means of central differences. The steady-state equations were solved in a pseudo-transient manner using an implicit Euler method in conjunction with a LUSGS method for solving the linear systems of equations. The 3v multigrid method was applied for convergence acceleration. Turbulence in these fully turbulent simulations was modeled with the Spalart–Allmaras turbulence model [18].

2.6 Engine model

The core engine was modelled with the engine boundary condition featured in the DLR TAU Code [17]. It links an inlet to an outlet surface and is regulated via a temperature and pressure ratio. Due to the core engine's comparatively low influence on the overall thrust of this UHBR engine, the simplification was made to keep the core engine boundary conditions constant across all degrees of embedding. The actuator disk model was used to model the counter-rotating fan efficiently. It models the effect of a rotor by a discontinuity surface that applies a change of momentum and energy to the airflow in a stationary form. The recently improved implementation of this model in the DLR TAU Code ensures that the flux conservative discretization across the discontinuity surface in the finite volume approach maintains second-order accuracy in space without introducing spurious oscillations, making it a robust and widely used model in the TAU code.

Figure 6 shows the actuator disk surfaces of the UHBR engine in the vertical plane along the engine centerline. The actuator disk model in connection with the blade element theory models the main effects of a rotor on the flow by means of a steady-state calculation. Compared to a transient calculation, which requires a temporal resolution of the blade movement and a spatial resolution of the blade geometry, the computational effort is reduced by about two orders of magnitude (see Table 4).

Figure 7 shows a propeller blade that rotates around the axis of rotation with the angular velocity Ω . The blade axis is the reference line for constructing the blade geometry.

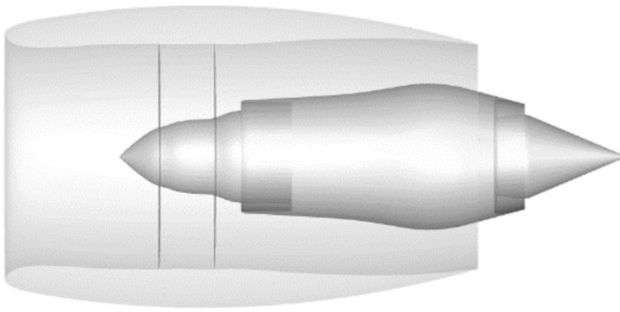


Fig. 6 Actuator disk model in AGATA^{3S} engine

Table 4 Reduced computational effort by two orders of magnitude

	AD	uRANS
Computing nodes	2	32
Computing cores	128	2048
Computing time (h)	12	336
Computing time (CPUh)	1536	668,128

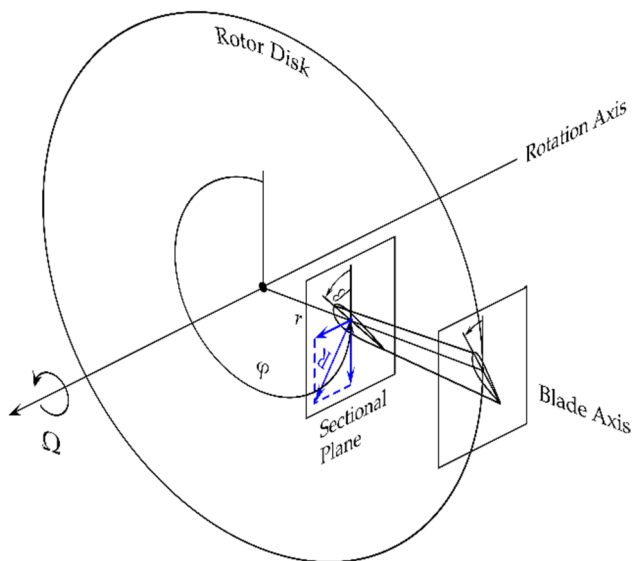


Fig. 7 Fundamentals of a rotating blade

The shape of the blade is defined by the profiles in the sectional planes perpendicular to the blade axis.

The actuator disk model neglects the width of the blade in the axial as well as the circumferential direction and represents the rotating blade by a rotating line. The area-specific forces acting on the blade surface are integrated over the blade profiles of the sectional planes, so that the distribution of the sectional loads acts as a length-specific force along the blade axis.

The sectional load at each point (r, φ) on the rotor disk is calculated from the flow condition and the properties of the profiles of the blade sections. These properties are the lift coefficient $C_L(\alpha)$ and the drag coefficient $C_D(\alpha)$ as a function of the angle of attack α . The angle of attack α is the angle between the chord and the inflow velocity vector.

The length-specific force of the rotating line acting on the rotor disk at a point (r, φ) can be converted into an equivalent steady-state surface specific force. This is achieved by normalizing the change in momentum imparted to the flow by the line element dr during an infinitesimal period of time dt with the swept over area and the time of revolution T . The imposition of an area-specific force on the surface of the propeller disk causes a discontinuous change in the flow condition.

The classic blade element theory considers a streamtube containing the flow that moves through a rotor. The flow condition is prescribed on a plane parallel to the rotor disk far in front of the rotor. The flow condition on a plane far behind the rotor can be calculated using momentum theory. In order to determine the flow condition on the rotor disk two vortex models are used, one for the axial and one for the circumferential direction.

The state of flow is known at the rotor disk, if the whole flow field is calculated numerically and the reaction of the pressure field of the actuator disk is taken into account. Therefore, the vortex model for the axial direction is not required.

The vortex model for the circumferential direction was switched off. In previous turbomachinery flow simulations, this method gave the best agreement between the transient rotating blade model and the actuator disk model [19]. This could be due to the lower development of tip vortices, since the shroud acts as a symmetry plane in the potential theory.

The actuator disk model of a propeller goes back to the early theories of W. J. M. Rankine and W. Froude, who investigated the function of screw propellers for ship propulsion. W. J. M. Rankine [20] introduced the momentum theory of a propeller in 1865, which was further developed by R. E. Froude [21]. He is credited with the concept of an ideal propeller in the form of an actuator disk, which causes a discontinuous change in the flow.

A comprehensive account of the development of the momentum theory and the blade element theory of a propeller can be found in [22]. Both theories compensate for the absence of the other, but were at odds with each other in their early stages of development. The momentum theory of a propeller and the blade element theory were originally developed for an incompressible flow. The system of equations for a discontinuous change of flow conditions in a compressible flow is described in [23]. The flux conservative discretization of an actuator disk as a discontinuity surface in a finite volume discretization is described in [24]. The

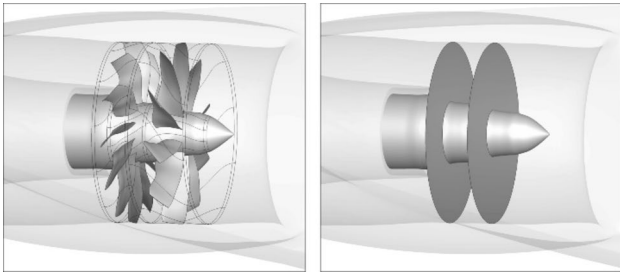


Fig. 8 Geometry for validation: uRANS (left), AD (right). For both DOE=30% and DOE=55%, good agreement was obtained in terms of mass flow and generated thrust

Table 5 AD validation against uRANS (cruise flight)

	\dot{m} [kg/s]	F_t [N]	Θ [-]	Π [-]	η_{is} [-]
AD ₃₀	311.8	30 · 250	1.076	1.265	0.913
AD ₅₅	300.2	27 · 885	1.071	1.247	0.918
uRANS ₃₀	310.2	30 · 827	1.084	1.276	0.854
uRANS ₅₅	302.1	27 · 543	1.078	1.248	0.835

discretization maintains second order accuracy in space without introducing spurious oscillations.

2.7 Actuator disk model setup and validation

The AD model requires both geometric and aerodynamic input data. The former consists of relative radius, relative cord length and blade angle at various locations along the blade axis. The latter includes the polar, i.e. the angle of attack α , the lift coefficient C_L and the drag coefficient C_D at 10%, 30%, 50%, 70% and 90% of the channel height. These polars were calculated by means of a 2D blade flow. The static pressure, the static temperature and the relative Mach number were required at the inlet. A static outlet pressure had to be specified at the outlet. The required thermodynamic reference values were extracted from a uRANS calculation with an identical operating point. The total channel length for the 2D calculation was 40 chord lengths. A periodic boundary condition was applied along the long side of the 2D domain to account for cascade effects between adjacent blades. The AD model was validated with the uRANS solution at DOE=30% and 55%. In the uRANS simulations, both rotors are fully geometrically represented (see Fig. 8). The unsteady flow phenomena of their rotation is accounted for in a time-accurate simulation approach [25]. This has been widely applied and validated for isolated and installed propeller, CROR (Contra-Rotating Open Rotor) [26] and turbofan propulsion systems [27].

Table 5 shows that these values differ by about 2%. For the uRANS simulation, the combined generated thrust of

all blades of the aft rotor was time averaged over one revolution. The angular resolution was 0.5° . Due to the gear ratio of both rotors, the thrust of the front rotor was time averaged over 1.26 revolutions. From the surface forces of the two rotors, the thrust was calculated using DLR's proprietary tool AeroForce (see Eq. 4). This does not follow to classic definition of thrust, because the division between engine and airplane is not easily possible with BLI.

$$F_{t,uRANS} = \frac{c_t \cdot A_{ref}^2 \cdot v_\infty}{2} \quad (4)$$

For the quasi-stationary AD simulation, the momentum introduced into the flow during an infinitesimal time span is related to the swept area and the rotational speed of the blade. The axial component of the resulting area-specific force on the surface of the actuator disk A_{AD} can be directly integrated into the thrust, using unit vector of the axis of rotation oriented in flight direction \vec{e}_a , the radial distance to the axis of rotation r as well as sectional load of the blade section, calculated from the curves of lift $C_L(\alpha)$ and drag $C_D(\alpha)$ (see Eq. 5).

$$F_{t,AD} = \vec{e}_a \iint_0^{A_{AD}} \frac{1}{2\pi r} \vec{f} dA \quad (5)$$

Furthermore, Table 5 shows that the deviation of the total pressure ratios Π as well as the total temperature ratios θ of the AD simulations is lower than 1% compared to the URANS simulations. For DOE=30%, the AD isentropic efficiency $\eta_{is,AD}$ is 6.9% higher and for DOE=50% the AD isentropic efficiency is 9.9% higher than the isentropic efficiencies of the uRANS simulations. The isentropic efficiency η_{is} is calculated using the adiabatic exponent κ , the total pressure ratio Π as well as the total temperature ratio T_{t2}/T_{t1} of the state of flow behind "2" and in front "1" of the fan:

$$\eta_{is} = \frac{\Pi^{\frac{\kappa-1}{\kappa}} - 1}{\frac{T_{t2}}{T_{t1}} - 1} \quad (6)$$

The AD model for a propeller simulation in a free flow typically shows a discrepancy of up to 5% compared to a uRANS simulation of a propeller with rotating blades. The larger discrepancy in this simulation of two rotor stages in a duct flow within an engine can be explained by the uncertainty in the determination the curves for the lift $C_L(\alpha)$ and drag $C_D(\alpha)$ for the individual blade sections making up the blade.

On one hand, the flow in the area of the rotor and the stator stage is conical. However, the blade sections, used to calculate the curves of lift and drag, were created and unwound on cylindrical surfaces concentric to the axis of rotation, introducing uncertainties. The curves of lift and

drag were then calculated for a staggered grid to take into account the mutual interaction of the blade sections.

Furthermore, the curves of lift and drag need to be calculated for a flow state with a positive pressure gradient in the flow direction. There are uncertainties in determining the correct counterpressure at the outlet.

With rotating blades, the shape of the curves of lift and drag deviates from the shape for a parallel inflow due to inertia effects in the boundary layer [28]. This leads to a much higher maximum angle of attack for attached flow at the expense of increased drag. Numerical simulations in [24] for a 1:5 SAAB SF340 model propeller showed a reduction in the gradient of the curve of lift and an increase of the gradient of the curve of drag in the region of attached flow, considering the inertial effects in the boundary layer. However, the inertial effects due to rotation were not taken into account in this investigation.

Additionally, in a uRANS simulation with rotating blades, vortices occur at the blade roots and blade tips, which reduce the efficiency of a rotor that cannot be considered with the actuator disk model.

3 Results

3.1 Inlet distortion coefficient (DC60)

The pressure distortion coefficient (DC) describes the magnitude of the flow non-uniformity caused by the BLI inlet distortion. It is calculated by the pressure difference between the mean total pressure and the average total pressure in a 60°-sector at each azimuthal position, normalized to the mean dynamic pressure q (see Fig 9 and Eq. (7)). The DC60 is the pressure ratio that is calculated by using the minimum averaged total pressure within a 60°-section (see Eq. (8)).

$$DC(\theta) = \frac{\overline{p_{tot}} - \overline{p_{tot,60^\circ,\varphi}}}{\overline{q}} \tag{7}$$

$$DC60 = \frac{\overline{p_{tot}} - \overline{p_{tot,60^\circ,min}}}{\overline{q}} \tag{8}$$

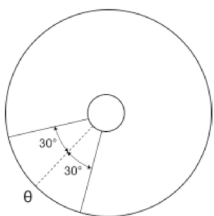


Fig. 9 DC60 definition

$$DC(\theta) = \frac{\overline{p_{tot}} - \overline{p_{tot,60^\circ,\varphi}}}{\overline{q}} \tag{7}$$

$$DC60 = \frac{\overline{p_{tot}} - \overline{p_{tot,60^\circ,min}}}{\overline{q}} \tag{8}$$

3.1.1 Inlet distortion at rotor 1

The extent and magnitude of the rotor 1 inlet distortion within every 60° cross section $p_{tot,60^\circ,\theta}$ is shown in Fig. 10.

Figure 10 shows that both the magnitude and the circumferential distribution of the inlet distortion increase along with the degree of embedding. For DOE=0 the total pressure loss is around 1000 Pa, the inverted bell curve stretching out across 120 degrees circumference. For DOE=55%, the total pressure loss is around 3500 Pa, with the corresponding bell curve stretching out across 195 degrees circumference.

Table 6 displays both the value and the corresponding circumferential position of the DC60 for each configuration. The DC60 increases steadily for greater degrees of embedding with the exception of the DC60 for DOE=55%. For this degree of embedding the DC60 value is slightly lower than the DC60 for DOE=50%. This is explained by a lower total pressure on the opposite side of the inlet distortion (see Fig. 11d), which is caused by a strong compression shock in the engine inlet (see Fig. 22).

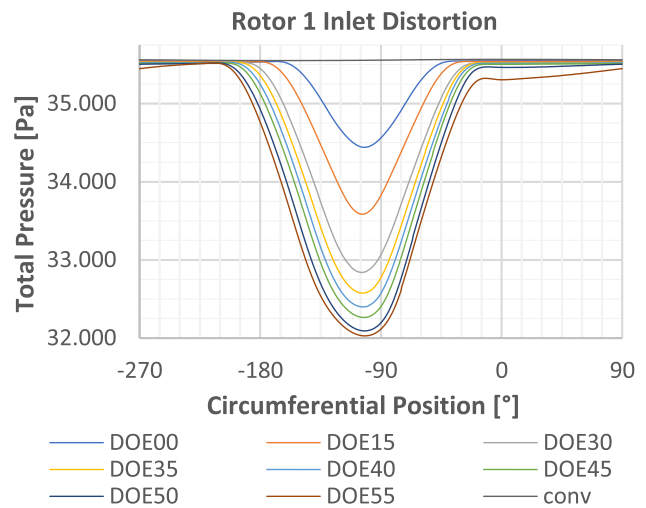


Fig. 10 Rotor 1 BLI inlet distortion $p_{tot,60^\circ,\theta}$

Table 6: Rotor 1 inlet distortion coefficient (DC60)

DOE	DC60	φ [°]
Conv	0.001	–
0	0.124	– 102.5
0.15	0.220	– 104.0
0.30	0.293	– 105.0
0.35	0.318	– 103.5
0.40	0.332	– 103.5
0.45	0.341	– 103.0
0.50	0.349	– 102.0
0.55	0.342	– 102.0

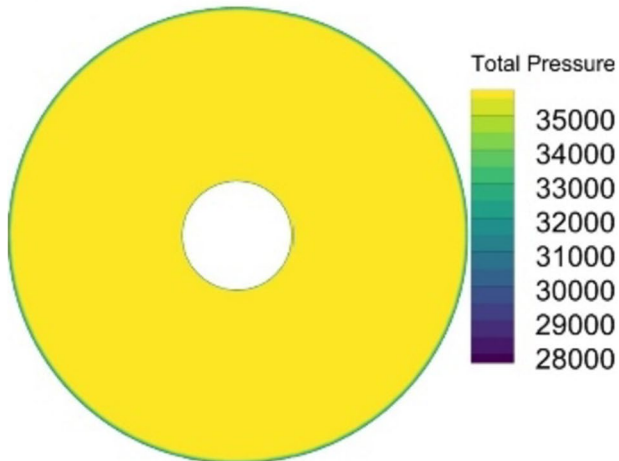
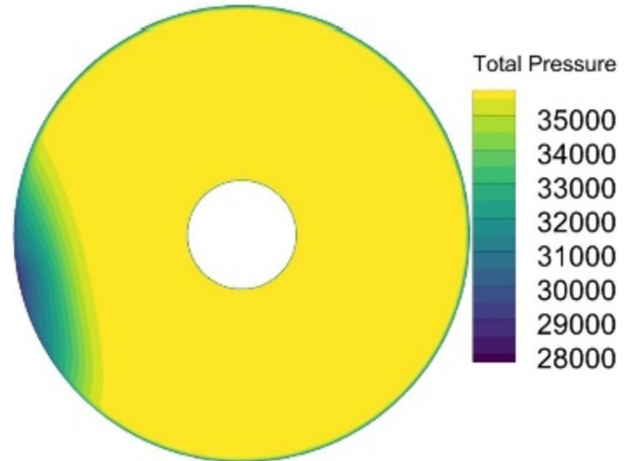
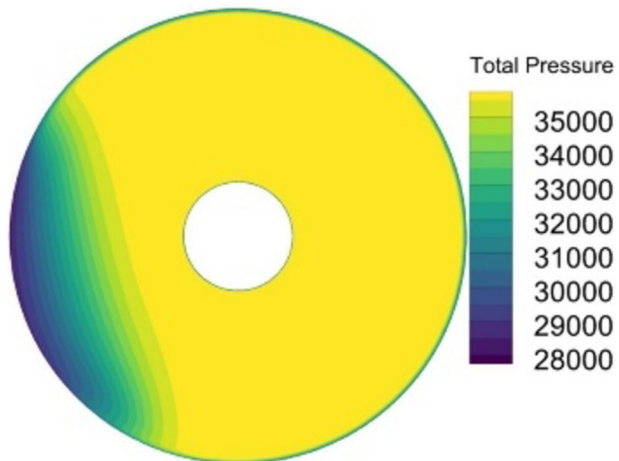
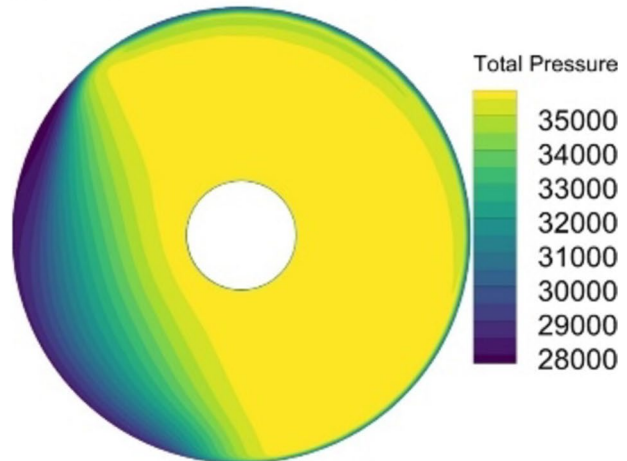
(a) Conventional Configuration**(b) Degree of Embedding = 0****(c) Degree of Embedding = 30%****(d) Degree of Embedding = 55%**

Fig. 11 Rotor 1 inlet distortions

Figure 11a–d gives an overview of the shape of the inlet distortion depending on the degree of embedding. The inlet distortions can lead to vibrational excitations of the rotor blades. Thus, when designing BLI aircraft, one key requirement is the design and development of distortion-tolerant fans, an effort that the work in the frame of the AGATA³⁵ project is aimed at supporting.

3.1.2 Inlet distortion at rotor 2

The magnitude of the rotor 2 inlet distortion within every 60° cross section $p_{tot,60^\circ,\theta}$ is shown in Fig. 12.

Figure 12 shows that the rotor 2 inlet distortion pressure losses for each DOE are only slightly lower than the inlet distortion pressure losses of rotor 1 (see Fig. 10). For DOE=0 the rotor 2 inlet distortion pressure loss is 65 Pa

lower than its rotor 1 equivalent, for DOE=50% the difference is reduced down to 27 Pa. The difference in inlet distortion pressure loss for DOE=55% is an exception to this trend with a total pressure difference of 183 Pa. This is because the inlet distortion is more mixed out for DOE=55%. Therefore, its inlet distortion pressure loss relative to the averaged pressure distribution decreases.

Figure 12 also shows that while the inlet distortion pressure losses remain similar to those of rotor 1 (see Fig. 10), they widen circumferentially, due to the swirl produced by rotor 1. This can be seen from the reduced gradients of the curves in Fig. 12 as well as the approximately 10% lower DC60 values of rotor 2 (see Table 7) compared to rotor 1 (see Table 6).

The more spread out inlet distortion downstream of rotor 1 leads to a reduction in the average total pressure

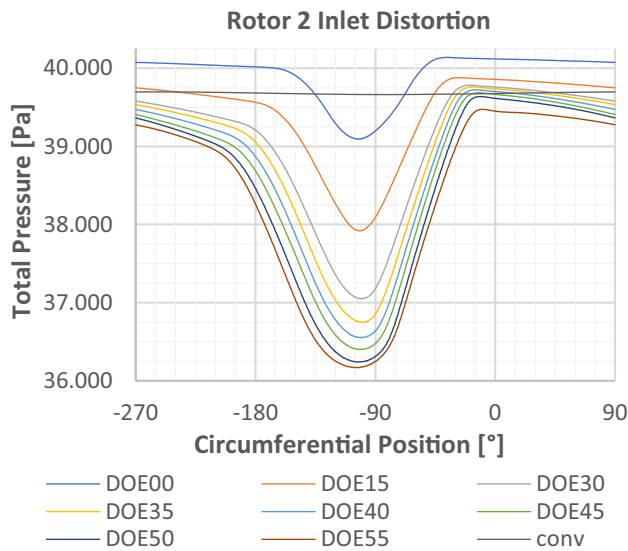


Fig. 12 Rotor 2 BLI inlet distortion $P_{tot,60^\circ,\theta}$

Table 7 Rotor 2 inlet distortion coefficient (DC60)

DOE	DC60	Θ [°]
Conv	0.003	–
0	0.110	– 103.0
0.15	0.205	101.5
0.30	0.275	– 100.5
0.35	0.298	– 100.0
0.40	0.308	– 101.5
0.45	0.313	– 101.5
0.50	0.316	– 101.5
0.55	0.306	– 102.5

P_{tot} according to Eq. (8). This results in lower DC60 values for rotor 2 (see Table 7) than for rotor 1 (see Table 6). The difference in these values is around 10% on average, so the design of distortion-tolerant fans is still required for rotor 2.

Figure 13 displays the more spread out characteristic of the inlet distortions in the outflow of rotor 1. While the inlet distortions widen in circumferential direction as they pass through rotor 1, their intensity remains largely the same compared to the inlet distortions in front of rotor 1 (see Fig. 11).

3.2 Shaft power for trimmed cruise flight

To quantify the benefit of BLI, comparisons were made to a conventional underwing configuration. The rotor speed was adjusted in such a way that a balance of forces was achieved and the aircraft moves with a uniform motion. The differences in required combined shaft power of the two rotors in each case show the power saving potential of BLI compared

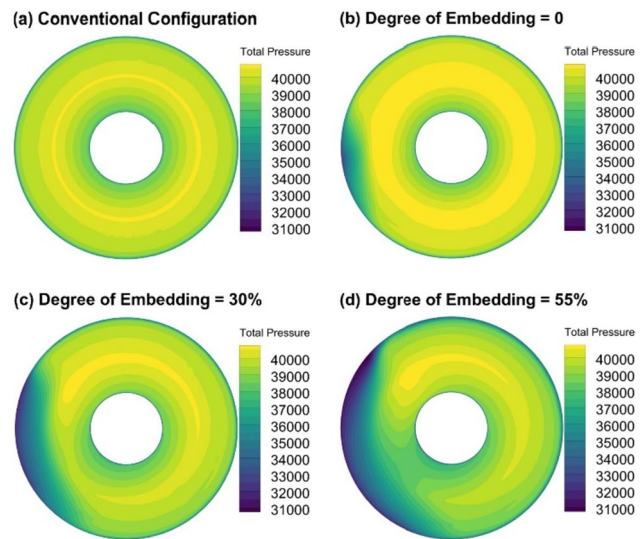


Fig. 13 Rotor 2 inlet distortions

to the underwing configuration. The power P generated by the engine was calculated using Eq. (9):

$$P = \sum_{i=1}^2 M_i \cdot \Omega_i \tag{9}$$

M_i denotes the moment a rotor exerts on the rotor axis. Ω_i denotes the angular velocity of the rotor. The core engine settings remained constant due to the core engine's negligible contribution to the overall thrust. Furthermore, the nacelle geometry remained rotationally symmetric throughout the study and no nacelle shape design was performed.

3.2.1 Total shaft power (rotor 1 and rotor 2)

The power saving potential of BLI is illustrated in Fig. 14. The horizontal axis shows the degree of embedding (DOE) as defined in Eq. (1). The vertical axis shows the combined shaft power as defined in Eq. (9). The larger the DOE, the smaller the shaft power required to maintain a trimmed cruise condition.

Smith [29] introduced the power saving coefficient (PSC):

$$PSC = \frac{P_{Conv} - P_{BLI}}{P_{Conv}} \tag{10}$$

P_{Conv} and P_{BLI} represent the combined shaft power required to propel the aircraft with and without BLI. The power saving coefficient PSC for the lowest degree of embedding DOE=0 is – 15.1%, so more shaft power is required to propel the BLI aircraft with the lowest degree of embedding than for the traditional underwing aircraft. This is due to compression shocks and aerodynamic losses

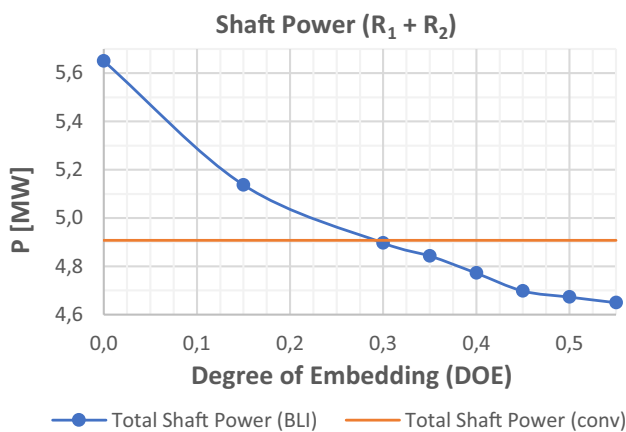


Fig. 14 Combined shaft power of Rotor 1 and Rotor 2

resulting from the non-optimized nacelle inlet geometry (see Figs. 20 and 21). The PSC for DOE = 55% is 5.3%, showing that there is power saving potential for this configuration. The break-even point is reached at DOE = 30%.

Its PSC result is not dissimilar to the 8.2% quoted in the D8 studies [3] and [4], but notably less than the power savings of 11–15% claimed for the STARC-ABL configuration [9]. The latter featured a tailcone-mounted aft propulsor ingesting the fuselage boundary layer in the full annulus. This, along with the design trades made possible by splitting thrust generation between the aft BLI engine and the underwing engines, probably explains the greater efficiency gains identified by NASA.

Its only slightly lower PSC reduction potential of the AGATA configuration compared to the D8 concept could also be partly due to the fact that the efficiency gains achievable through the ingestion of the boundary layer on the flat upper surface of this configuration should be greater. Furthermore, the scope of work in AGATA did not allow for an optimization of the airframe and specifically the engine integration for the numerous degrees of embedding studied. As will be discussed in Sect. 4, some particularly detrimental transonic flow phenomena associated with the specifics of engine-airframe integration at certain DOEs cause losses that are also reflected in a reduction in achievable PSC improvement. With an appropriately modified AGATA aircraft design, it is expected that the power saving potential should be consistent with the D8 studies.

3.2.2 Shaft power (rotor 1)

Figure 15 shows the required shaft power for rotor 1 for each configuration

For rotor 1, the PSC for DOE = 55% is 6.8%, which shows that the power saving potential is greater for rotor 1 than for the combined fan stages (see Fig. 14). It follows that the

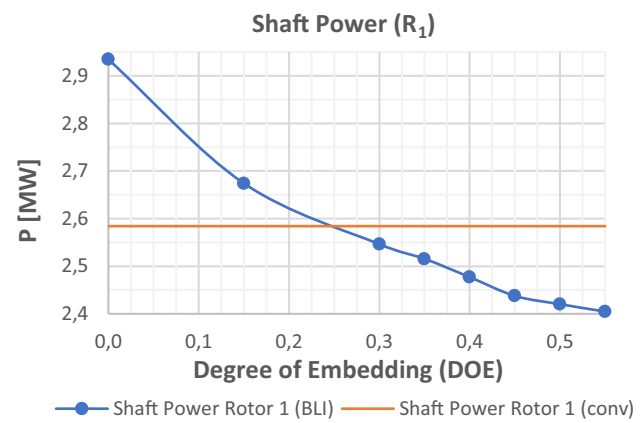


Fig. 15 Rotor 1 shaft power consumption

shaft power of rotor 1 is proportionally reduced more than the shaft power of rotor 2. This change in load distribution can be explained by the different inflow conditions for each rotor that are characterized by inlet distortions of different shapes and intensities. These alter the inflow conditions for each rotor in terms of velocity, density, temperature and total pressure, thereby shifting their respective operating points on the compressor map and altering the shaft power distribution. As discussed in Sect. 3.1, the slightly more pronounced inlet distortion effects seen by the front rotor are likely the main cause for a larger change in this rotors' operating point than seen for the aft rotor.

3.2.3 Shaft power (rotor 2)

Figure 16 displays the required shaft power for rotor 2 for each configuration.

For rotor 2, the PSC for DOE = 55% is 3.5%, which shows that the power saving potential is lower for rotor 2 than for the combined fan stages. The break-even point is approximately at DOE = 35%. This is reflected by the fact that the ratio of the shaft power requirement differs

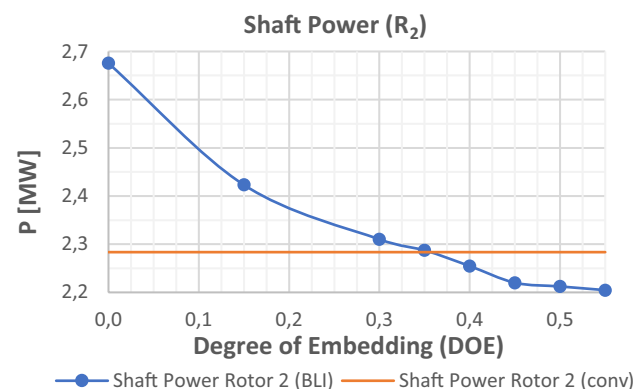


Fig. 16 Rotor 2 shaft power consumption

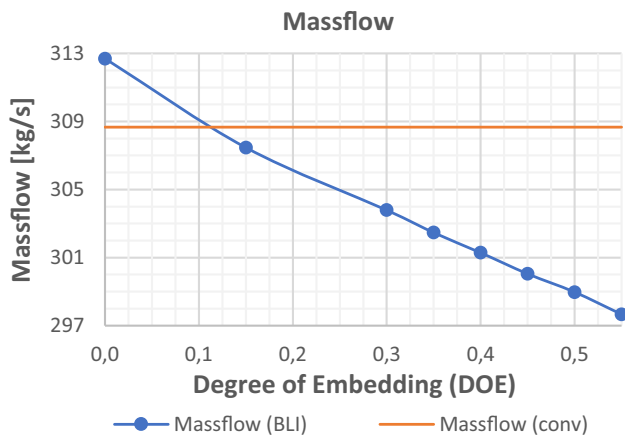


Fig. 17 Engine mass flow rate

between the conventional underwing configuration and the BLI configurations. For the former, rotor 1 requires 6.9% more shaft power than rotor 2. For the latter, rotor 1 only requires 5.2–5.7% more shaft power, so the balance of required shaft power shifts slightly toward rotor 2 for BLI configurations as explained in chapter 3.2.2.

3.3 Engine mass flow rate

Figure 17 shows that the greater the degree of embedding, the lower the engine mass flow.

The mass flow rate for $DOE=0$ is 1.3% higher than the mass flow rate for the conventional underwing configuration, while the mass flow rate of $DOE=55\%$ is 3.6% lower than the mass flow rate of the conventional underwing configuration. The main reason for this is the reduced thrust requirement for greater DOEs due to decreased drag.

3.4 Fan pressure ratio

Figure 18 shows that the greater the DOE, the lower the fan pressure ratio

The fan pressure ratio for $DOE=0$ is 2.3% higher than the fan pressure ratio for the conventional underwing configuration, while the fan pressure ratio of $DOE=55\%$ is 0.16% lower than fan pressure ratio of the conventional underwing configuration. It is important to note that the engine diameter remained the same for all DOEs and no design adjustments were made. As DOEs increase, the wetted surfaces decrease, reducing the overall drag and, therefore, the thrust required. The lower thrust requirement was met by reducing the rotor speed, which in turn led to a lower engine mass flow.

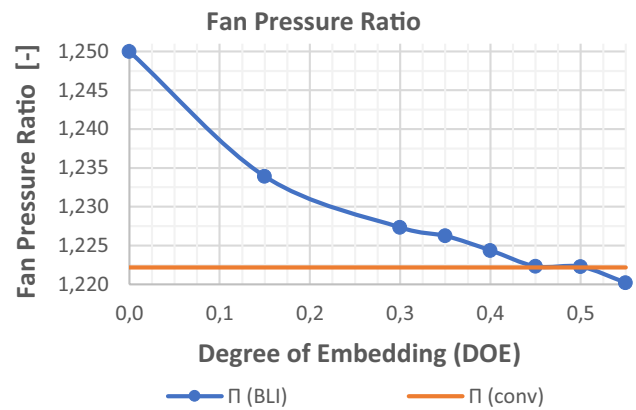


Fig. 18 Fan pressure ratio

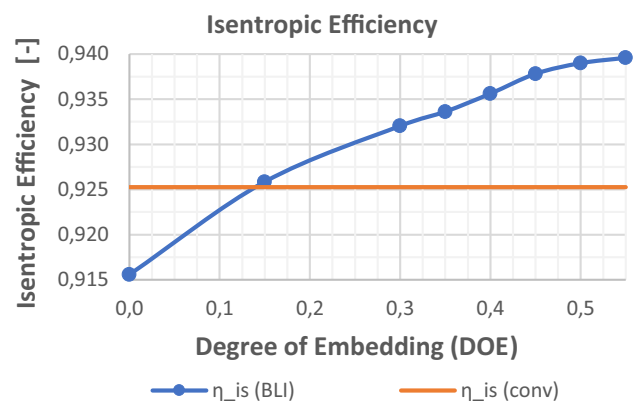
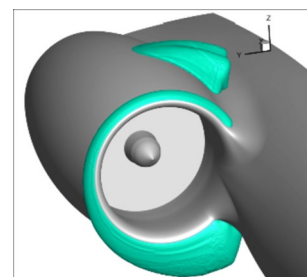


Fig. 19 Isentropic efficiency

Fig. 20 $Ma=1$ isosurface showing supersonic flow regions, $DOE=0$, iso-view

3.5 Isentropic Efficiency

Figure 19 shows that the greater the DOE, the greater the isentropic efficiency η_{is} .

The isentropic efficiency for $DOE=0$ is 1.0% lower than the isentropic efficiency for the conventional underwing configuration, while the isentropic efficiency of $DOE=55\%$ is 1.5% higher than the isentropic efficiency

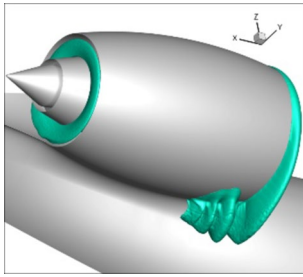


Fig. 21 $Ma=1$ isosurface showing supersonic flow regions, DOE=0, rear-bottom view

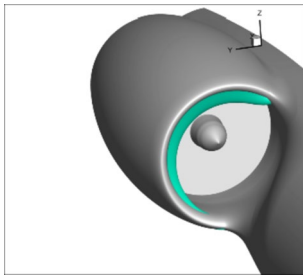


Fig. 22 $Ma=1$ isosurface showing supersonic flow regions, DOE=0.55, iso-view

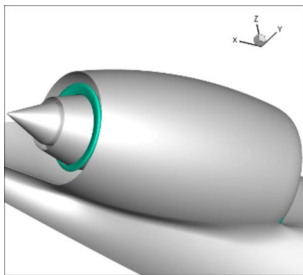


Fig. 23 $Ma=1$ isosurface showing supersonic flow regions, DOE=0.55, rear-bottom view

of the conventional underwing configuration. The higher isentropic efficiency is due to the higher proportion of ingested boundary layer as well as the lower massflow required to achieve a balance of forces, reducing the required increase of kinetic energy in the jet required for propulsion. For the validation simulations discussed in chapter 2.7, a fixed engine operating point was used with an identical farfield state. This operating point featured higher rotor speeds for both DOE 0.3 and 0.55 than those used for this BLI study. These were not adjusted to achieve a balance of forces and can, therefore, not be compared with the series of simulations investigating the DOE impact shown in Fig. 19.

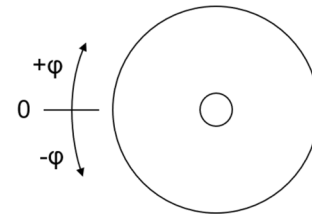


Fig. 24 Sketch of the azimuthal angle definition

4 Aerodynamic analysis

This engine performance analysis is merely an initial result, as it is based on non-optimized aircraft geometries. Both in the CFD simulations with the BLI configuration and in the calculation with the underwing configuration there are potentially avoidable shocks and losses in and around the nacelle. A fair comparison would require a more refined design or optimization of the various engine-airframe configurations, which was outside the scope of the present studies in AGATA³⁵.

4.1 Aerodynamic effects on the BLI aircraft

The main aerodynamic losses transpire due to compression shocks that occur for all BLI configurations, but vary depending on the degree of embedding. At low degrees of embedding, they occur around the nacelle lip mainly on the underside as well as in the channel formed by the nacelle and upper fuselage (see Figs. 20 and 21).

As the degree of embedding increases, the compression shocks on the outside of the nacelle disappear and shocks occur in the engine inlet (see Figs. 22 and 23).

This shows that the aircraft's aerodynamic performance is critically determined by the geometry of the fuselage and the nacelle due to their strong mutual interaction. Therefore, the aerodynamic design for fuselage and nacelle geometry must be performed together for each degree of embedding. Much more so than for the underwing configuration, the BLI configurations do not allow for a separate design of the engine and the rest of the aircraft.

4.2 Stagnation line

A circular stagnation line is formed on the lip of the nacelle by the streamtube of air ingested by the engine. The position of the circular stagnation line depends on the BLI geometry of the integrated engine, which largely depends on the degree of embedding. The definition of the azimuthal angle along the intake lip used in the analysis of the stagnation line is shown in Fig. 24.

The azimuthal position of $\varphi = 0$ is set as the outboard, non-embedded section of the engine. The positive angles

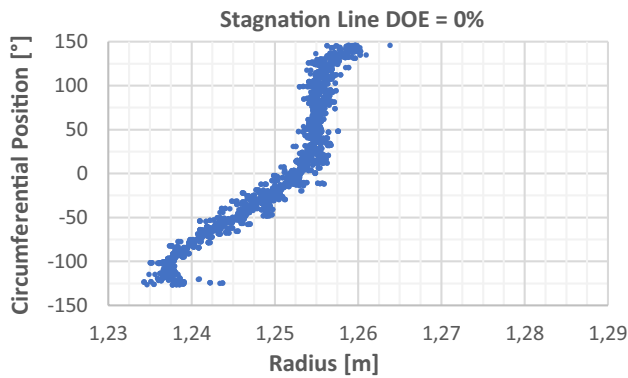


Fig. 25 Stagnation line for DOE=0%

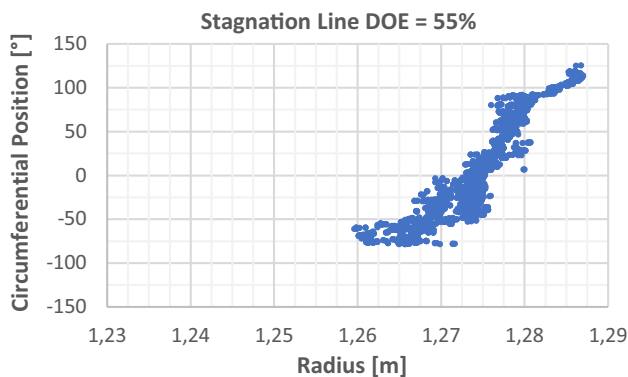


Fig. 26 Stagnation line for DOE=55%

represent the top of the nacelle lip, whereas the negative angles represent its lower portion. The point clouds in Figs. 25 and 26, showing stagnation point locations in terms of radius and azimuth, are the result of an evaluation using the DLR developed aerodynamic analysis and post-processing tool AeroForce [30]. When more of the nacelle is embedded in the fuselage, the remaining circular arc of the nacelle lip becomes smaller, resulting in a shorter stagnation line (see Fig. 25).

In general, an ideal nacelle design would feature a stagnation line at the leading edge of the nacelle lip for the design conditions, avoiding excessive flow acceleration either into the intake or, for the external flow, around the nacelle. However, the stagnation lines for DOE=0 (see Fig. 25), DOE=55% (see Fig. 26) have a varying radius. This is because an identical nacelle geometry was used throughout the BLI study, resulting in two main trends:

1. The greater the degree of embedding, the greater the radius at a given circumferential location. This is due to the increasing proportion of relatively slow boundary layer flow, representing essentially a partial blockage of the inlet. In order to compensate for the reduced

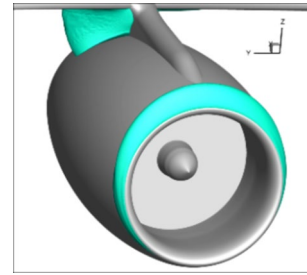


Fig. 27 Ma=1 isosurface showing supersonic flow regions, underwing aircraft, iso view

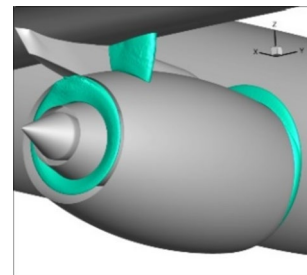


Fig. 28 Ma=1 isosurface showing supersonic flow regions, underwing aircraft, rear view

inflow area, a larger air massflow is required through the remaining intake area, resulting in the shift of the stagnation line to larger radii.

2. For smaller azimuthal angles, i.e. the lower portion of the inlet, the stagnation line generally shifts to smaller radial locations, more on the inside of the intake. This results in a high acceleration of the flow around the outer lip and leads to the compression shock on the underside of the nacelle (see Figs. 25, 26 and 20). The stagnation lines seen for the degrees of embedding in between the extreme cases shown in Figs. 20 and 22 follow these trends but are not shown for reasons of space.

The different stagnation line radii indicate that an asymmetric engine intake geometry must be used to achieve less adverse flow around the engine lip. This requires a complex three-dimensional aerodynamic design. These findings can help inform future research to design a more optimized engine-airframe integration for these types of BLI engine configurations.

4.3 Aerodynamic effects on the conventional underwing aircraft

In the underwing configuration simulation, compression shocks occur on the top of the nacelle lip and in the area between the wing and the nacelle (see Figs. 27 and 28).

The nacelle lip and the overall intake shape design need to be optimized for the critical flight conditions to avoid the associated aerodynamic losses. A common aerodynamic design of the pylon, wing and nacelle is necessary to avoid the compression shock between the top of the nacelle and the wing. The closer the engine is to the wing, the stronger the interactions and the greater the demands on the integrated design.

5 Summary and outlook

In this investigation, a study was conducted to evaluate the energy saving potential of BLI aircraft versus conventional underwing configurations. Eight BLI configurations with different degrees of embedding were compared in a thrust-trimmed cruise flight condition at a constant lift coefficient. The results indicate that overall aircraft performance improvements can be expected for BLI configurations. The required shaft power of the highest degree of embedding (DOE = 55%) is 5.3% lower than the required shaft power of the conventional underwing configuration, with a break-even point seen for a DOE = 30% in this study.

A final quantification of the engine power saving potential requires further engine-airframe integration design refinements, as compression shocks and aerodynamic losses in and on the nacelle occurred due to the use of a fixed nacelle geometry. Potentially, the degree of embedding required to achieve an advantage with respect to the reference underwing-mounted engine configuration could be lower, as more significant loss-associated aerodynamic flow features were seen for the smaller DOEs, which could thus benefit from a more optimized shape design.

Different degrees of embedding result in inlet distortions of varying magnitudes and the analysis presented in this paper can help to support the design of distortion-tolerant fans. While the BLI studies mentioned in Sect. 3.2.1 showed a greater power saving potential, this study provides a detailed insight into the flow physics in and around the engine. It focuses on identifying critical areas and shows where shape optimizations need to be made to achieve greater power saving benefits. The results of this study will be a good starting point for future design studies of BLI concepts. Future work should aim at the optimization of the engine-airframe integration for the aircraft configurations used in this study. This would allow for a more definitive determination of the overall performance benefits that are achievable through the use of BLI-ingesting engines.

Funding Open Access funding enabled and organized by Projekt DEAL.

Declarations

Conflict of interest The authors have no conflicts of interest to disclose.

Open Access This article is licensed under a Creative Commons Attribution 4.0 International License, which permits use, sharing, adaptation, distribution and reproduction in any medium or format, as long as you give appropriate credit to the original author(s) and the source, provide a link to the Creative Commons licence, and indicate if changes were made. The images or other third party material in this article are included in the article's Creative Commons licence, unless indicated otherwise in a credit line to the material. If material is not included in the article's Creative Commons licence and your intended use is not permitted by statutory regulation or exceeds the permitted use, you will need to obtain permission directly from the copyright holder. To view a copy of this licence, visit <http://creativecommons.org/licenses/by/4.0/>.

References

1. European Commission: ACARE Flightpath 2050—Europe's vision for aviation (2017). <https://www.acare4europe.org/acare-goals/>.
2. Yutko, B., Titchener, N., Chambers, J. T., Courtin, C., Lieu, M., Roberts, T., Tylko, J., Wirsing, L.: Conceptual design of a D8 commercial aircraft. In: AIAA Paper No. 2017-2254 (2017)
3. Uranga, A., Drela, M., Greitzer, E. M., Hall, D. K., Titchener, N. A., Lieu, M. K., Siu, N. M., Casses, C., Huang, A. C., Gatlin, G. M., Hannon, J. A.: Boundary layer ingestion benefit of the D8 transport aircraft. *AIAA J.* **55**(11) (2017)
4. Uranga, A., Drela, M., Hall, D. K., Greitzer, E. M.: Analysis of the aerodynamic benefit from boundary layer ingestion for transport aircraft. *AIAA J.* **56**(11) (2018)
5. Wiart, L., Atinault, O., Paluch, B., Hue, D., Grenon, R.: Development of NOVA aircraft configurations for large engine integration studies. In: AIAA, Paper No. 2015-2254 (2015)
6. Isikveren, A.T., Seitz, A., Bijewitz, J., Mirzoyan, A., Isyanov, A., Grenon, R., Atinault, O., Godard, J.L., Stueckl, S.: Distributed propulsion and ultra-high by-pass rotor study at aircraft level. *Aeronaut. J.* **119**(1221), 1327–1376 (2015)
7. Seitz, A., Peter, F., Bijewitz, J., Habermann, A., Goraj, Z., Kowalski, M., Pardo, A. C., Hall, C., Meller, F., Merkle, R., Petit, O., Samuelsson, S., Corte, B. D.: Concept validation study for fuselage wake filling propulsion integration. In: 31st Congress of the International Council of the Aeronautical Sciences, Paper No. ICAS 2018_0342, Belo Horizonte, Brazil (2018)
8. Welstead, J. R., Felder, J. L.: Conceptual design of a single-aisle turboelectric commercial transport with fuselage boundary layer ingestion. In: AIAA, Paper No. 2016-1027 (2016)
9. Yildirim, A., Gray, J. S., Mader, C. A., Martins, J. R. R. A.: Boundary-layer ingestion benefit for the STARC-ABL concept. *J. Aircraft* **59**(4) (2022)
10. Engelbrecht, E. G., Gkoutzamanis, V. G., Nasoulis, C. P., Kalfas, A. I.: Inlet flow distortion dependencies for tail mounted ducted fans on hybrid-electric commuter aircraft. In: ASME Turbo Expo, GT2022-80894, Rotterdam, The Netherlands (2022)
11. Felder, J. L., Brown, G. V., Kim, H. D., Chu, J.: Turboelectric distributed propulsion in a hybrid wing body aircraft. In: 20th International Society for Airbreathing Engines, Paper No. ISABE 2011-1340, Gothenburg, Sweden (2011)
12. Schmollgruber, P., Doell, C., Hermetz, J., Liaboef, R., Ridel, M., Cafarelli, I., Atinault, O., Francois, C., Paluch, B.: Multidisciplinary Exploration of dragON: an onera hybrid electric distributed propulsion concept. In: AIAA, Paper No. 2019-1585 (2019)

13. Seitz, A., Hübner, A., Risse, K.: The DLR tulam project: design of a short and medium range transport aircraft with forward swept NLF wing. *CEAS Aeronaut. J.* **11**(449–459), 2019 (2020)
14. Lengyel-Kampmann, T., Otten, T., Schmidt, T., Nicke, E.: Optimization of an engine with a gear driven counter rotating fan—Part I: fan performance and design. In: *ISABE-2015–20091* (2015)
15. Federal Aviation Administration: Design considerations for minimizing hazards caused by uncontained turbine engine and auxiliary power unit rotor failure,” AC 20–128A (1997)
16. Software: CENTAUR Grid Generator, <https://www.centaurosoft.com/>, Austin, Texas
17. Gerhold, T.: Overview of the hybrid RANS TAU-code, pp. 81–92. Springer, Berlin Heidelberg (2005)
18. Spalart, P. R., Allmaras, S. R.: A one-equation turbulence model for aerodynamic flows. In: *AIAA Paper 92–0439* (1992)
19. Spinner, S., Keller, D., Trost, M., Schnell, R.: A blade element theory based actuator disk methodology for modeling of fan engines in RANS simulations. *AIAA*, Orlando (2020)
20. Rankine, W. J. M.: On the mechanical principles of the action of propellers. In: *Transactions of the Institution of Naval Architects*, Vol. 6, London, pp. 13–39 (1865)
21. Froude, R. E.: On the part played in propulsion. In: Holmes, G. (ed) *Transactions of the institution of naval architects*, Vol. 30, , London, pp. 390–405 (1889)
22. Glauert, H.: Airplane propellers. In: Durand, W.F. (ed.) *Division L of aerodynamic theory, a general review of progress*, vol. IV, pp. 169–360. Julius Springer, Berlin (1935)
23. Horlock, J.H.: *Actuator disk theory—discontinuities in thermo-fluid dynamics*. McGraw-Hill, London (1978)
24. Raichle, A.: Flusskonservative diskretisierung des wirkscheibenmodells als unstetigkeitsfläche. In: *Dissertation Technische Universität Braunschweig, DLR-Forschungsbericht 2017–62, NFL-Forschungsbericht 2017–26, ISSN 1434–8454, ISRN DLR-FB-2017–62, Braunschweig* (2017)
25. Stürmer, A.: DLR TAU-Code uRANS turbofan modeling for aircraft aerodynamics investigations. *Aerospace* **6**(121), 1–22. <https://doi.org/10.3390/aerospace6110121>. (Multidisciplinary Digital Publishing Institute (MDPI), ISSN 2226–4310)
26. Stürmer, A., Akkermans, R.: Validation of aerodynamic and aeroacoustic simulations of contra-rotating open rotors at low-speed flight conditions, Atlanta, Georgia. *AIAA Aviation*, USA (2014)
27. Roosenboom, E., Stürmer, A., Schröder, A.: Advanced experimental and numerical validation and analysis of propeller slipstream flows. *J. Aircraft* **47**: 284–291 (2010). <https://doi.org/10.2514/1.45961>. (American Institute of Aeronautics and Astronautics, ISSN 0021–8669).
28. Himmelskamp, H.: Profile investigations on a rotating airscrew. In: *Reports and Translations No 832, AVA 45 A20, Aerodynamische Versuchsanstalt, Göttingen* (1947)
29. Smith, L.H.: Wake ingestion propulsion benefit. *J. Propul. Power* **9**(1), 74–82 (1993)
30. Wild, J.: AeroForce—thrust/drag bookkeeping and aerodynamic force breakdown over components. In: *German Aerospace Center; DLR-IB-AS-BS-2018–51, Braunschweig* (2018)

Publisher's Note Springer Nature remains neutral with regard to jurisdictional claims in published maps and institutional affiliations.